HAL open science

Effects of surface rigidity and metallicity on dielectric properties and ion interactions at aqueous hydrophobic interfaces

Philip Loche, Laura Scalfi, Mustakim Ali Amu, Otto Schullian, Douwe Bonthuis, Benjamin Rotenberg, Roland Netz

To cite this version:

Philip Loche, Laura Scalfi, Mustakim Ali Amu, Otto Schullian, Douwe Bonthuis, et al.. Effects of surface rigidity and metallicity on dielectric properties and ion interactions at aqueous hydrophobic interfaces. The Journal of Chemical Physics, 2022, 157 (9), pp.094707. 10.1063/5.0101509 . hal-03798804

HAL Id: hal-03798804

https://hal.science/hal-03798804

Submitted on 5 Oct 2022

HAL is a multi-disciplinary open access archive for the deposit and dissemination of scientific research documents, whether they are published or not. The documents may come from teaching and research institutions in France or abroad, or from public or private research centers.

L'archive ouverte pluridisciplinaire **HAL**, est destinée au dépôt et à la diffusion de documents scientifiques de niveau recherche, publiés ou non, émanant des établissements d'enseignement et de recherche français ou étrangers, des laboratoires publics ou privés.

Effects of surface rigidity and metallicity on dielectric properties and ion interactions at aqueous hydrophobic interfaces

Philip Loche,[1,2] Laura Scalfi,[2,3] Mustakim Ali Amu,[3] Otto Schullian,[2]
Douwe J. Bonthuis,[4] Benjamin Rotenberg,[3] and Roland R. Netz[2,*]

[1] *Laboratory of Computational Science and Modeling, IMX, École Polytechnique Fédérale de Lausanne, 1015 Lausanne, Switzerland*
[2] *Fachbereich Physik, Freie Universität Berlin, 14195 Berlin, Germany*
[3] *Physicochimie des Électrolytes et Nanosystèmes Interfaciaux, CNRS 8234, Sorbonne Université, F-75005 Paris, France*
[4] *Institute of Theoretical and Computational Physics, Graz University of Technology, 8010 Graz, Austria*

(Dated: October 5, 2022)

Using classical molecular dynamics simulations we investigate the dielectric properties at interfaces of water with graphene, graphite, hexane and water vapor. For graphite we compare metallic and non-metallic versions. At the vapor-liquid water and hexane-water interfaces the laterally averaged dielectric profiles are significantly broadened due to interfacial roughness and only slightly anisotropic. In contrast, at the rigid graphene surface the dielectric profiles are strongly anisotropic and the perpendicular dielectric profile exhibits pronounced oscillations and sign changes. The interfacial dielectric excess, characterized by the shift of the dielectric-dividing-surface with respect to the Gibbs-dividing-surface, is positive for all surfaces, showing that water has an enhanced dielectric response at hydrophobic surfaces. The dielectric-dividing-surface positions vary significantly among the different surfaces, which points to pronounced surface-specific dielectric behavior. The interfacial repulsion of a chloride ion is shown to be dominated by electrostatic interactions for the soft fluid-fluid interfaces and by non-electrostatic Lennard-Jones interactions for the rigid graphene-water interface. A linear tensorial dielectric model for the ion-interface interaction with sharp dielectric interfaces located on the dielectric-dividing-surface positions works well for graphene but fails for vapor and hexane, because these interfaces are smeared out. The repulsion of chloride from the metallic and non-metallic graphite versions differs very little, which reflects the almost identical interfacial water structure and can be understood based on linear continuum dielectric theory. Interface flexibility shows up mostly in the non-linear Coulomb part of the ion-interface interaction, which changes significantly close to the interfaces and signals the breakdown of linear dielectric continuum theory.

INTRODUCTION

Electrostatic forces play a major role in the interactions between matter on the nano-scale and consequently determine the macroscopic behavior of many materials. Electrostatic interactions between charged objects such as lipid membranes, proteins, molecules and ions are profoundly influenced by the surrounding water[1]. On the linear response level, the time-averaged effect of water on electrostatic interactions is quantified through the static dielectric constant ε, which is spatially constant in homogeneous bulk systems and reduces the force between two charges by a factor of 80 compared to vacuum. Close to an interface, however, the effect of water on electrostatic interactions is more intricate. The water density near an interface deviates from its bulk value and the proximity of a surface restricts the molecular conformations. Therefore, it is not surprising that interfacial water has a different structure and a different dielectric response compared to bulk, as was shown in molecular simulations as well as in experiments [2–11]. The change of the dielectric properties has a pronounced influence on the behavior of ions at interfaces [12] and for example influences their distribution at solid [13, 14] as well as fluid (i.e., liquid-liquid or liquid-vapor) interfaces [15, 16], but also fundamentally influences the transport of ions across interfaces, in particular between an aqueous and an apolar phase [17]. Studying the distribution and transport of ions and charged molecules is of fundamental importance in various fields of physics, chemistry and biology, from heterogeneous catalysis to ion extraction and from electrochemical applications like energy storage to drug delivery [18–22]. For understanding the influence of interfacial water effects on charged objects, the determination of their solvation free energy profile across interfaces is of great importance, because the free energy profile represents the thermodynamic driving force for transport. The free energy itself is influenced by non-electrostatic as well as electrostatic contributions, where the latter are fundamentally determined by the dielectric water properties at the interface.

To shed light on the water properties at hydrophobic planar interfaces, we here use molecular dynamics simulations and investigate the interfacial dielectric behavior as well as the free-energy profile of chloride ions at different aqueous interfaces. In order to disentangle the effects of rigidity and metallicity of the surface, we

investigate metallic as well as non-metallic versions of graphite, which is a very rigid surface, and treat vapor-water (short for vapor-liquid water) and hexane-water interfaces, which are two examples of soft fluid interfaces, as well as the graphene-water interface, which again is rigid. Using previously developed methods for extracting the spatially resolved dielectric tensor [6, 9, 23], we find pronounced differences in the dielectric water response at the different surfaces, which reflect varying dielectric interfacial excesses that can be explained by shifted positions of the dielectric dividing surface (DDS). By splitting the ionic free-energy profiles into electrostatic and non-electrostatic Lennard Jones (LJ) contributions, we find that the repulsion of ions from an interface is dominated by the electrostatic contribution for fluid interfaces and by the non-electrostatic contribution at solid interfaces, in agreement with previous findings for a thiocyanate ion [24]. Not surprisingly, a sharp dielectric-interface model for the ionic free-energy profile fails for the fluid interfaces, which are characterized by broad and smeared-out dielectric response profiles for both perpendicular and parallel directions. Furthermore, by expanding the Coulomb part of the ionic free energy profile in powers of the ionic charge, we demonstrate that for all interfaces, non-linear dielectric effects, as quantified by higher-order expansion coefficients, are modified significantly as the ion approaches the surface. However, the magnitudes of the different non-linear components are different for each interface type, which can be understood by symmetry arguments: The cubic contribution is similar for all surface types and accounts for the non-linear coupling between ionic hydration and water orientation at the planar interface, the quartic contribution differs between different surface types and accounts for interface deformation, in particular at the soft fluid-fluid interfaces. The dielectric model for the quadratic part fails for vapor and hexane because the interfaces are smeared out (not because they are flexible), interface flexibility shows up mostly in the quartic contribution. Surprisingly, the metallic nature of graphite only plays a marginal role for the interfacial water structure and the interfacial free energy profile of single ions. Deep in the vapor or the hexane phase, we find that several solvating water molecules stay bound to a chloride and sodium ion in equilibrium, with the average number of hydration waters being different for chloride and sodium and for vapor and hexane.

METHODS

We simulate interfaces between liquid water and water vapor, hexane, graphene, and metallic and non-metallic graphite. For water the non-polarizable SPC/E model is used [25]. Production runs are executed in the NVT ensemble at a temperature of $T = 300\,\mathrm{K}$. The first set of simulations is without ions. In a second set we add a chloride or a sodium ion with a charge $q = \mp e$ at variable positions as well as a sodium or a fluoride counter ion, respectively, fixed in the center of the water slab, which avoids artifacts in charged inhomogeneous systems [26], the interaction of the ion with its counterion and all periodic images is subtracted using analytical expressions. Ion LJ parameters are taken from Ref. 27.

The simulation box of the vapor-water system has an extension of $5.1\,\mathrm{nm} \times 5.4\,\mathrm{nm} \times 70\,\mathrm{nm}$ and contains 9024 water molecules that spontaneously form a liquid-water slab with a thickness of roughly 10 nm and a vapor phase with a thickness of roughly 60 nm. To avoid motion of the water slab towards the ion, we apply a harmonic force on the center of mass of the system in the z direction with a force constant $1000\,\mathrm{kJ} \cdot \mathrm{mol}^{-1} \cdot \mathrm{nm}^{-2}$. It was shown previously [28] that such a force has no detectable effect on the structure and the dynamics of the water slab.

The hexane-water system has an extension of $4\,\mathrm{nm} \times 4\,\mathrm{nm} \times 12.5\,\mathrm{nm}$ and contains 2000 water molecules and 630 hexane molecules. The hexane is modeled with all-atomistic OPLS force fields [29] and thus carries constant partial charges. Before production runs, the phase-separated system is equilibrated for 1 ns in the NPT ensemble at 1 bar pressure. The water slab thickness is roughly 5 nm. The non-aqueous phases of the vapor-water and the hexane-water systems are saturated with water molecules, as discussed below.

The graphene-water system has an extension of $5.1\,\mathrm{nm} \times 5.4\,\mathrm{nm} \times 70\,\mathrm{nm}$, where the water is confined between two graphene sheets with a separation of 9.9 nm. The carbon atoms are frozen in space and non-polarizable and do not carry any charge, the graphene sheets are therefore non-metallic. We adjust the water number between the graphene slabs to a value of 8701 molecules, for which the water chemical potential equals the bulk value of $(-11.706 \pm 0.003)\,\mathrm{k_B T}$ [30].

All simulations above are performed using the GROMACS molecular dynamics simulation package [31] and the systems are periodically replicated in all directions. In the case of the vapor-water and the graphene-water interfaces, a slab-correction is used [32].

We also simulate metallic and non-metallic versions of graphite using the MetalWalls molecular dynamics simulation package [33], employing periodic boundary conditions in lateral directions only. For the metallic system a constant electric-potential boundary condition is used on one of the two graphite slabs, while the second graphite slab is treated as non-metallic. In these simulations, the charge on the carbon atoms is allowed to fluctuate with the constraints of a constant electric potential at the atomic positions and global electroneutrality [34]. The electrolyte is treated with constant point charges and creates a fluctuating electric field, which in turn determines the polarization charges on the metallic surface atoms. The metallic graphite-water system has an extension of $3.41\,\mathrm{nm} \times 3.69\,\mathrm{nm}$, with a separation be-

tween the graphite slabs of 5.51 nm. Each graphite slab is composed of $n = 3$ graphene sheets with a separation of 0.3354 nm consisting of 480 carbon atoms per sheet and 2071 water molecules in between. Graphite is used instead of graphene to ensure that the induced charges in the metallic slab decay to zero on the third sheet. As for the graphene systems, all carbon atoms are frozen in space and the water number is chosen so that the water density in bulk equals the one for the graphene system. All force field parameters are identical to the graphene systems. For direct comparison, the same system is also run treating both graphite slabs as non-metallic but keeping all other parameters the same.

Further information about the methods and simulation details are given in section S1 in the Supplemental Information.

RESULTS AND DISCUSSION

Dielectric properties

Figure 1 shows profiles of the total mass density $\rho_m(z)$, the parallel dielectric response $\varepsilon_\parallel(z)$, the inverse perpendicular dielectric response $\varepsilon_\perp^{-1}(z)$ as well as the laterally averaged electrostatic potential $\varphi(z)$ for the water-vapor, water-hexane and water-graphene systems. All profiles are shifted according to the Gibbs dividing surface (GDS) that is based on the water mass density profiles and shown by the vertical black dotted line in Fig. 1d, that means, $z = 0$ denotes the GDS position for all systems. The water phase is located in the right half-space ($z > 0$) whereas the non-aqueous phase is located in the left half-space ($z < 0$). Figures 1a–c show simulation snapshots of the three systems and illustrate that the interfacial water layer is highly corrugated at the vapor and hexane interfaces, while it is perfectly flat at the rigid graphene sheet. $\rho_m(z)$ shown in Fig. 1d exhibits the expected sigmoidal shape for the liquid vapor-water and hexane-water systems with a broadening that originates mostly from the intrinsic interfacial water roughness and to a lesser extent from capillary waves [35]. In contrast, $\rho_m(z)$ of the graphene system shows the typical oscillations due to water layering at rigid flat interfaces and a peak at $z = -0.19$ nm due to the graphene sheet. In section S3 of the supplemental information, we show that the water-vapor interfacial profiles are reproduced rather well by convoluting the graphene profiles with an interface position distribution. This suggests that local details at the water-vapor interface are to some degree smeared out by interface corrugation and capillary fluctuation effects [35].

The parallel $\varepsilon_\parallel(z)$ and the inverse perpendicular $\varepsilon_\perp^{-1}(z)$ dielectric profiles for the fluid vapor-water and hexane-water interfaces show sigmoidal shapes that are qualitatively similar to the shapes of the corresponding mass

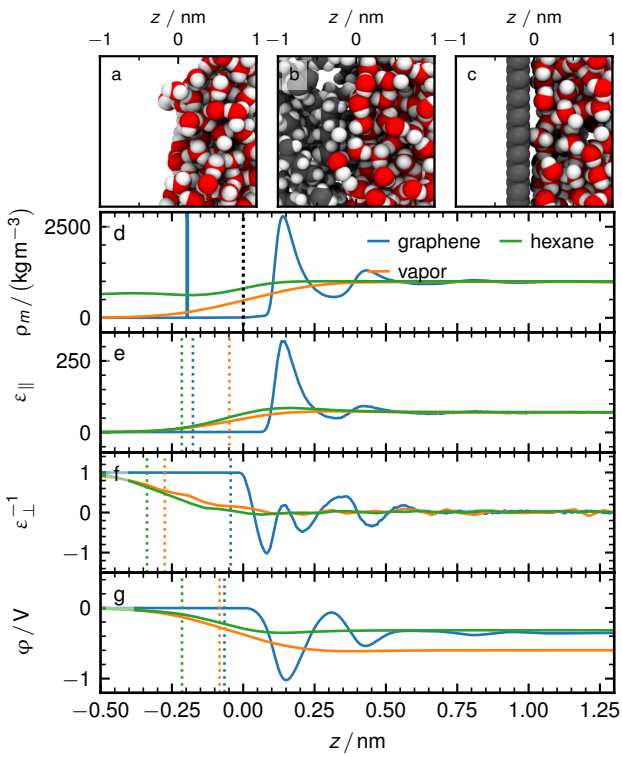

Figure 1. Simulation snapshots for (a) the vapor-liquid water system, (b) the hexane-water system, (c) the graphene-water system. Profiles for (d) the total mass density $\rho_m(z)$, (e) the parallel dielectric response $\varepsilon_\parallel(z)$, (f) the inverse perpendicular dielectric response $\varepsilon_\perp^{-1}(z)$ and (g) the laterally averaged electrostatic potential $\varphi(z)$. The coordinate z denotes the distance from the Gibbs dividing surface and vertical dotted lines in (e) and (f) indicate dielectric dividing surface positions and in (g) the potential dividing surface positions. The peak at $z = -0.19$ nm in (d) stems from the frozen graphene layer.

density profiles. The parallel profile $\varepsilon_\parallel(z)$ for graphene exhibits pronounced maxima and is roughly proportional to the corresponding mass density profile, but the perpendicular profile $\varepsilon_\perp^{-1}(z)$ shows multiple sign-changes and is not related to the water mass density profile near the graphene wall in any simple manner [6, 9]. Note that the sign changes of $\varepsilon_\perp^{-1}(z)$ reflect divergencies of $\varepsilon_\perp(z)$, a clear indication of overscreening at rigid surfaces, which is only observed for the perpendicular component [6, 9]. The vertical dashed lines in Fig. 1e-f depict the DDS positions, which are constructed analogously to the Gibbs dividing surface (see eq. (S4) in the supplemental information) and quantify the dielectric excess of each interface. We see that the DDS for all systems and for both parallel and perpendicular directions is located to the left of the GDS, meaning that the dielectric interfacial excess is generally positive; in other words, water at hydrophobic surfaces has a higher dielectric response per water molecule at the interface than in bulk. The location of

the DDS is different for each system and the ordering of the three systems does not agree between the parallel and perpendicular directions. Whereas for the parallel component the ordering from left to right is hexane, graphene, vapor, meaning that hexane has the highest and vapor the smallest surface excess, the ordering for the perpendicular component is hexane, vapor, graphene, meaning that graphene has the lowest excess. A high dielectric excess means that the dielectric screening of a charge close to the interface is strong, which in turn leads to reduced electrostatic interactions. It transpires that interfacial electrostatics is expected to be weakest for hexane for a fixed location relative to the GDS, but due to the different ordering of the parallel and perpendicular components of graphene and vapor it is not clear whether the graphene-water or the vapor-water system shows the strongest electrostatic interactions at the interface (a point we will come back to further below). In summary, we find pronounced anisotropy of the dielectric interfacial behavior, not only are the parallel and perpendicular dielectric profiles very different, also the parallel and perpendicular DDS positions are different and there does not seem to be a simple correlation of the DDS positions with the rigidity of the interface. The only trend we can discern is that for soft interfaces, the parallel DDS is closer to the GDS than the perpendicular DDS, whereas the opposite behavior is found for the rigid graphene surface.

Fig. 1g shows the laterally averaged electrostatic potential $\varphi(z) = -\int_{-\infty}^{z} \mathrm{d}z' \int_{-\infty}^{z'} \rho(z'')\mathrm{d}z''/\varepsilon_0$, obtained by integrating twice over the charge density profile $\rho(z)$ due to the water (and hexane where applicable) partial charges. We see that the potential for the graphene system shows pronounced oscillations, which seem correlated to the density and the parallel dielectric profiles but not to the perpendicular dielectric profile. In contrast, the potential in the fluid systems changes monotonically. The potential consists of a dipolar contribution due to interfacial water ordering and a quadrupolar contribution that is only weakly dependent on the interfacial water ordering [6]. We see that the potential in the water bulk is negative for all systems but differs considerably between the different systems; the vapor-water system reaches a potential of $\varphi(z \to \infty) = -0.6$ V far from the interface, while for the graphene and the hexane systems we find reduced values of $\varphi(z \to \infty) = -0.38$ V and $\varphi(z \to \infty) = -0.37$ V, respectively. In fact, the negative sign is produced by the dominant negative quadrupolar water contribution, which is an intrinsic water property and depends sensitively on the water force field but is independent of the interfacial structure; in *ab initio* simulations the quadrupolar water contribution has a positive sign, as has been amply discussed in the literature [36, 37]. The dipolar contribution due to water interfacial orientation is less dependent on the water force field, therefore the difference in the total potential seen in Fig. 1g is expected to be a robust feature of these systems, indicating that the orientational interfacial water ordering is more pronounced for vapor compared to graphene and hexane. Note that $\varphi(z)$ is the electrostatic potential experienced by an infinitesimally small test charge that laterally averages over the entire water phase (including the interior of the water molecules) and is therefore unrelated to the electrochemical potential experienced by an ion, as will be discussed further below.

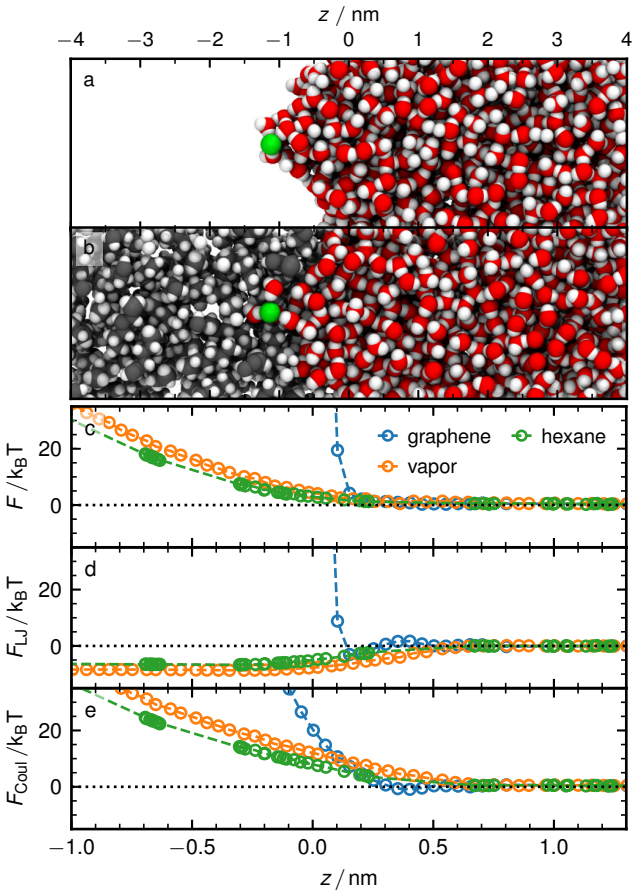

Figure 2. Simulation snapshots of a chloride ion at a position $z = -1.0$ nm relative to (a) the vapor-liquid water interface and (b) the hexane-water interface. A water finger that engulfs the ion is clearly visible. (c) Total free energy profiles $F = F_{\mathrm{LJ}} + F_{\mathrm{Coul}}$ for the three different interfacial systems and their (d) LJ contributions F_{LJ} and (e) Coulomb contributions F_{Coul}.

Ion-interface free energy

Obviously, the interfacial dielectric properties influence the interfacial ion solvation and the ionic interaction with an interface, but since an ion significantly perturbs the interfacial water structure and possibly induces non-linear

dielectric effects, it is not clear to what extent dielectric profiles are sufficient to predict the ion free energy close to an interface. We thus place a chloride ion at variable positions relative to the interface and extract its free energy profile using thermodynamic integration (TI), as done previously in Ref. 38. Figure 2 shows the free energy profiles $F(z)$ for the vapor, hexane and graphene systems, where the reference point $F = 0$ is located in the center of the water slab. Fig. 2c shows the total free energy profile $F(z) = F_{\mathrm{LJ}}(z)+F_{\mathrm{Coul}}(z)$, while in Fig. 2d–e the separate Lennard-Jones and Coulomb contributions are shown, which are subsequently obtained from thermodynamic integration (see SI section S1 E). In other words, $F_{\mathrm{LJ}}(z)$ is the free energy profile of an uncharged LJ sphere, while $F_{\mathrm{Coul}}(z)$ is the free energy needed for charging the sphere, thus both $F_{\mathrm{LJ}}(z)$ and $F_{\mathrm{Coul}}(z)$ contain contributions from LJ as well as Coulomb interactions. We find that $F(z)$ is repulsive for all three systems. The decomposition demonstrates that the interplay between the LJ and Coulomb contributions is dramatically different for the systems. While the total free energy is dominated by repulsive Coulomb interactions for the vapor-water and hexane-water systems, it is dominated by repulsive LJ interactions for the graphene-water system.

As the ion approaches the vapor-water and hexane-water interfaces, the Coulomb contribution in Fig. 2e increases monotonically, which is due to interfacial polarization effects and corresponds to image-charge repulsion in a simple continuum dielectric model [39]. In contrast, the Lennard-Jones contribution in Fig. 2d becomes attractive if the ion approaches the vapor or hexane phase, which is caused by the positive (i.e. unfavorable) solvation free energy of a Lennard-Jones sphere in water [40–42]. Note that for negative z values, we observe the formation of a water finger around the ion in the vapor and hexane phases, as shown in Fig. 2a–b and reported previously for vapor [28, 43–46] and organic solvents [43, 44]. The hexane phase produces a lower total free energy for $z < 0$, because of a less repulsive Coulomb contribution. This can only partly be rationalized by the slightly higher bulk dielectric constant of our non-polarizable hexane force-field model ($\varepsilon_{\mathrm{hexane}} = 1.01$ from Fig. 1) compared to water vapor (see SI section S1 B for details). We also find that $F_{\mathrm{LJ}}(z)$ in the hexane phase is slightly more repulsive than in vapor, which one could be tempted to associate with the different LJ interaction parameters between chloride and hexane, $\sigma_{\mathrm{Cl,Hex}} = 0.4\,\mathrm{nm}$ and $\epsilon_{\mathrm{Cl,Hex}} = 0.34\,\mathrm{kJ\,mol^{-1}}$, and between hexane and hexane, $\sigma_{\mathrm{Hex,Hex}} = 0.35\,\mathrm{nm}$ and $\epsilon_{\mathrm{Hex,Hex}} = 0.28\,\mathrm{kJ\,mol^{-1}}$. However, based on the larger chloride-hexane LJ interaction parameter $\epsilon_{\mathrm{Cl,Hex}}$ compared with the hexane-hexane parameter $\epsilon_{\mathrm{Hex,Hex}}$, one would expect the net LJ solvation free energy to be more favorable in hexane compared to vapor. We conclude that the different total solvation free energies of a chloride ion in hexane and vapor must be related to details of the microscopic solvation structure in hexane and vapor, as will be discussed further below. In contrast to the hexane and vapor systems, and as previously shown in Ref. 38, the total free energy for graphene is dominated by the Lennard-Jones repulsion, as seen in Fig. 2d.

Finally, comparing the Coulomb contributions for each surface type in Fig. 2e, we find that at the graphene interface the Coulomb contribution increases most steeply, which is related to the different water mass density profiles at the different surfaces, being very smooth for the fluid interfaces and rather sharp for the graphene layer, as shown in Fig. 1d. A second difference between the systems is that the ion looses solvating water molecules as it approaches the graphene layer, while for the vapor and hexane systems, the formation of a water finger maintains a complete hydration shell around the ion even when the ion crosses the GDS, which results in a reduced Coulomb free-energy repulsion in the non-aqueous phase.

Ion hydration in vapor and hexane phases

If the ion moves further away from the interface into the vapor or the hexane phase, the water finger breaks but the ion stays hydrated by a water solvation shell that consists of a few water molecules [28, 45, 46]. The solvating water molecules are in equilibrium with the water-saturated vapor or hexane phase and with the water bulk phase. From simulations without an ion, we obtain for the vapor phase a water number density of $c_{\mathrm{vap}} = 7\cdot 10^{-4}$ nm^{-3}, which corresponds to an ideal gas pressure of $P_{\mathrm{vap}} = 30\,\mathrm{mbar}$, slightly lower than the experimental water vapor pressure of $P_{\mathrm{vap}} = 42\,\mathrm{mbar}$ at 300 K [47]. For the hexane-water system we find a slightly lower but comparable water concentration of $c_{\mathrm{hex}} = 5.9\cdot 10^{-4}\ \mathrm{nm}^{-3}$ in the hexane phase, in good agreement with the experimental value $c_{\mathrm{hex}} = 6.3 \cdot 10^{-4}\ \mathrm{nm}^{-3}$ [48] and leading to a corresponding partial water pressure in the hexane phase of $P_{\mathrm{hex}} = 24\,\mathrm{mbar}$ based on the ideal gas equation. See SI Fig. S2 for a time series of the number of water molecules in the vapor phase.

The equilibrium properties of the water solvation shell around an ion in the non-aqueous phase is investigated in separate simulations by fixing an ion sufficiently far from the interface at a distance of $z = -7.0\,\mathrm{nm}$ in the vapor or hexane phase. The simulation snapshots in Figs. 3a-d demonstrate the accumulation of hydration water around an ion over time, starting initially with an unhydrated ion configuration. Figures 3e-f show the number of water molecules $N_{\mathrm{H_2O}}$ in a spherical shell of radius 1 nm around a chloride and a sodium ion as a function of time, again starting with an initially unhydrated ion. The data demonstrate that chloride and sodium attract roughly the same number of water molecules in their hydration shell, which suggests a similar hydration free energy of

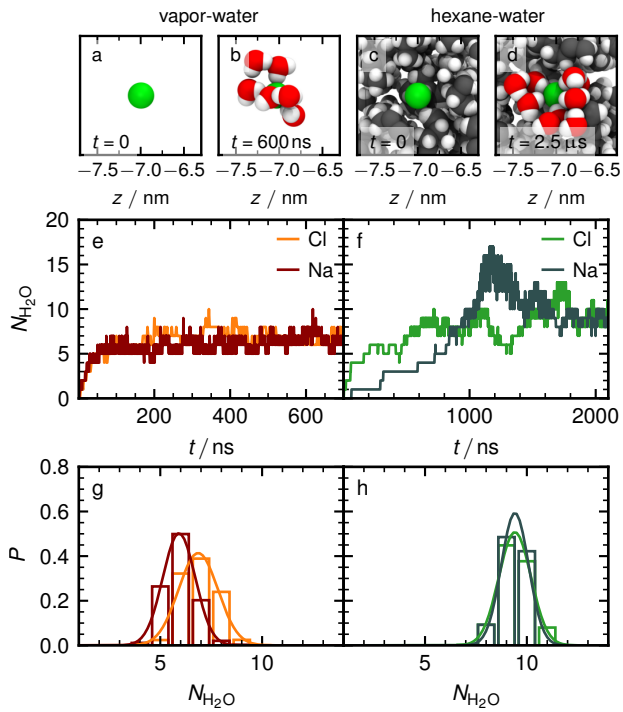

Figure 3. (a–d) Snapshots for the initial and final configurations of a chloride ion in vapor and hexane, respectively. Number of water molecules $N_{\mathrm{H_2O}}$ in a sphere with radius 1 nm around the ion at a fixed position $z = -7.0$ nm as a function of time for the (e) vapor-water system and the (f) hexane-water system. (g, h) Corresponding distribution of $N_{\mathrm{H_2O}}$, discarding the initial 100 ns of 650 ns for the vapor-water systems and the initial 1.8μs of 2.1μs for the hexane-water systems. Lines are Gaussian fits from which the free energy for $N_{\mathrm{H_2O}} = 0$ is obtained by extrapolation and given in Tab. I. The mean value of the Gaussian fits for the sodium ion is 5.9 solvating water molecules in vapor and 9.4 in hexane, while for the chloride ion it is 6.9 solvating water molecules in vapor and 9.4 in hexane.

the two ions. In section S1 C of the SI we demonstrate that all hydrating water molecules bind within a single hydration shell around each ion. Additionally, we show in section S6 of the SI that the ion hydration structure at the water-vapor interface using the TIP4P/ε water force field [49] is comparable to the structure obtained for the SPC/E force field, which is used for all our results.

We rationalize these results by an analysis of the binding free energy of a single water molecule onto an ion [28]. The hydrating water molecule is described by the partial oxygen charge, q_O, located at a distance $B_{\mathrm{O},i}$ from the ion i, and the partial hydrogen charges $q_H = -q_O/2$ at a distance of $B_{\mathrm{H},i}$ from the ion center, see insets in Fig. 4 for a schematic description of the hydration model. The hydration free energy is the sum of the Coulomb free energy and the translational and rotational entropy losses

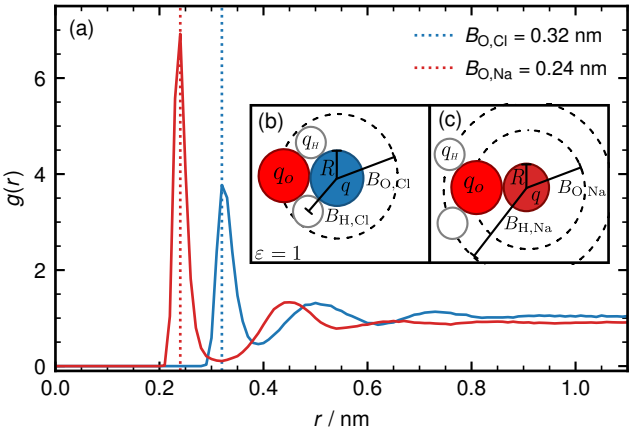

Figure 4. (a): Chloride-oxygen (blue) and sodium-oxygen (red) radial distribution function $g(r)$ obtained from bulk water simulations containing a single Cl or Na ion. (b,c): Geometric model for the binding of a single water molecule to a chloride or sodium ion.

upon water binding to an ion,

$$\frac{U_{\mathrm{bind}}}{k_{\mathrm{B}}T} = \frac{U_{\mathrm{Coul}}}{k_{\mathrm{B}}T} + S_{\mathrm{trans}} + S_{\mathrm{rot}} = -l_{\mathrm{B}}^{\mathrm{vac}}|qq_O|\left|\frac{1}{B_{\mathrm{H},i}} - \frac{1}{B_{\mathrm{O},i}}\right| + \ln\left(\frac{v_{\mathrm{naq},j}}{v_{\mathrm{hyd},i}}\right) + S_{\mathrm{rot}}\,, \tag{1}$$

where $v_{\mathrm{naq},j}$ is the molecular water volume either in fully saturated vapor, $v_{\mathrm{naq,vapor}} = 1/c_{\mathrm{vap}} = 1415\,\mathrm{nm}^{-3}$, or in hexane, $v_{\mathrm{naq,hexane}} = 1/c_{\mathrm{hex}} = 1698\,\mathrm{nm}^{-3}$ (see SI section S1 B), and $v_{\mathrm{hyd,i}} = 4\pi B_{O,i}^3/3$ is the approximate hydration volume, i.e., the volume available for a hydrating water molecule. We estimate the chloride-oxygen distance as $B_{\mathrm{O,Cl}} = 0.32$ nm and the sodium-oxygen distance as $B_{\mathrm{O,Na}} = 0.24$ nm from the radial distribution functions $g(r)$ in liquid water shown in Fig. 4. Additionally, $B_{\mathrm{H,Cl}} = 0.27$ nm and $B_{\mathrm{H,Na}} = 0.40$ nm are calculated using the SPC/E geometric parameters [25] (see section S4 for details on the calculations). Using the SPC/E partial charges we find $U_{\mathrm{Coul}}/k_{\mathrm{B}}T \approx -24$ for chloride and ≈ -44 for sodium. The translational entropy is $S_{\mathrm{trans}} \approx 11$ regardless whether the ion is chloride or sodium and the surrounding medium is vapor or hexane, see SI table S2 for the exact values. The rotational entropy loss upon water binding has been estimated as $S_{\mathrm{rot}} \approx 2$ for a similar system [50]. In conclusion, the Coulomb free energy in Eq. (1) outweighs the entropy loss and we estimate a favorable hydration free energy of about $U_{\mathrm{bind}} \approx -11\,k_{\mathrm{B}}T$ for the first water molecule that adsorbs onto a chloride ion. For the sodium ion we find a much larger binding energy of $U_{\mathrm{bind}} \approx -31\,k_{\mathrm{B}}T$. The negative energy corroborates our simulation result that chloride and sodium are hydrated in saturated water vapor and hexane. Note that the binding free energy of sub-

Table I. Estimate of the hydration free energy of chloride and sodium ions F_0 in the vapor and hexane phase, in units of k_BT, by extrapolation of the Gaussian fits for the water hydration number given in eq. (2) and shown in Fig. 3g-h.

	Vapor	Hexane
Cl^-	26 ± 2	72 ± 2
Na^+	28 ± 1	99 ± 5

sequently adsorbing water molecules will be reduced due to Coulomb repulsion between water molecules. That the number of adsorbing water molecules is roughly the same for chloride and sodium ions indicates that the first hydration shell around both ions has roughly the same size and that a second hydration is free-energetically unstable.

We find from our simulations in Fig. 3e-f that the number of hydration waters in hexane is slightly larger compared to vapor. This cannot be explained within our simple binding model for a single water molecule and is most likely due to the different structure of the hydration shell in vapor and hexane and related to the reduced interfacial tension between water and hexane compared to vapor. Additionally, we note that the equilibration time for the hydration shell in Fig. 3e-f is much longer in hexane compared to vapor, which is due to the low diffusivity of individual water molecules in hexane compared to vapor.

From the distribution of N_{H_2O} shown in Fig. 3g-h and Gaussian fits according to

$$P(N_{H_2O}) = \frac{1}{\sigma\sqrt{2\pi}} e^{-\frac{1}{2}\left(\frac{N_{H_2O}-\mu}{\sigma}\right)^2}, \qquad (2)$$

we extrapolate $P(N_{H_2O})$ to $N_{H_2O} = 0$ and thereby extract the hydration free energy of the ions according to $F_0 = -k_BT \ln P(0)$ in the hexane and in the vapor phase. The results are given in Table I. The fit results are subject to large errors due to statistical noise in the simulated distributions and also because of possible non-Gaussian contributions to the distribution for $N_{H_2O} \to 0$. Nevertheless, we find as a trend that i) the solvation free energy F_0 in the hexane phase is substantially larger (i.e. more favorable) compared to the vapor phase and ii) F_0 is slightly larger for sodium compared to chloride. The second trend is related to the smaller size of the sodium ion, which leads to a stronger hydration of sodium compared to chloride, as also follows from our simple ion-water binding model above. The first trend is in line with the larger number of hydration waters in hexane compared to vapor and, as mentioned above, most likely caused by a reduced interfacial tension between the hydration shell and the surrounding hexane molecules compared to vapor.

Metallic versus non-metallic graphite

Many surfaces are metallic, meaning that charges in the environment induce surface charges such that the potential is constant inside the metal. This also holds for some carbon-based materials such as graphene and graphite. One would expect that surface metallicity has a strong influence on the interfacial water structure and the interactions with ions, since water partial charges and ionic charges will interact with polarization charges on the metal. In order to check for such effects, we perform constant-potential simulations for metallic graphite, where the charges on the metallic atoms are allowed to fluctuate in response to the fluctuating electric field created by the electrolyte (for more details see the Methods section and section S1 in the Supplemental Information). Note that the water and ions have constant charges and thus no charge transfer is allowed between the electrolyte and the metallic surface. For comparison, we also perform simulations for non-metallic graphite.

In Fig. 5 we compare our results for metallic and non-metallic graphite, where we also add results for non-metallic graphene for comparison that we discussed before. We note that the LJ force-field parameters and the lateral carbon lattice structure of graphene and both graphite versions are exactly the same. In Fig. 5a-b we show simulation snapshots for the non-metallic and metallic graphite-slab versions, respectively, with the charges on the carbon atoms indicated by color. It is clearly seen that for the metallic graphite, the negative chloride ion induces a positive local surface charge, while a water hydrogen atom close to the surface induces a negative local surface charge. Panels (c–f) show structural properties at the interface, namely the water mass density $\rho_m(z)$, the number density $\rho_N(z)$ of the oxygen and hydrogen atoms (where the hydrogen density is divided by two for comparison with the oxygen density), the charge density $\rho(z)$ as well as the mean cosine of the angle between the water dipole moment and the surface normal, $\cos(\theta)$. The profiles for the three different surfaces look very similar and are characterized by a strongly enhanced water density and pronounced orientational ordering in the first hydration layer. Water molecules right at the surface point their hydrogen atoms toward the surface, $\cos(\theta) < 0$, followed by water molecules within the density maximum that point their oxygens toward the surface, $\cos(\theta) > 0$. In particular, we observe only marginal differences in the profiles between metallic and non-metallic graphite, in agreement with previous reports [51–54]: A slightly stronger orientation of the first water layer on metallic graphite can be deduced from the larger hydrogen number density for $z < 0.05$ nm in Fig. 5d and from the more negative average $\cos(\theta)$ close to the GDS for $z < 0.15$ nm in Fig. 5f.

In Fig. 5g we compare the free-energy profile for a

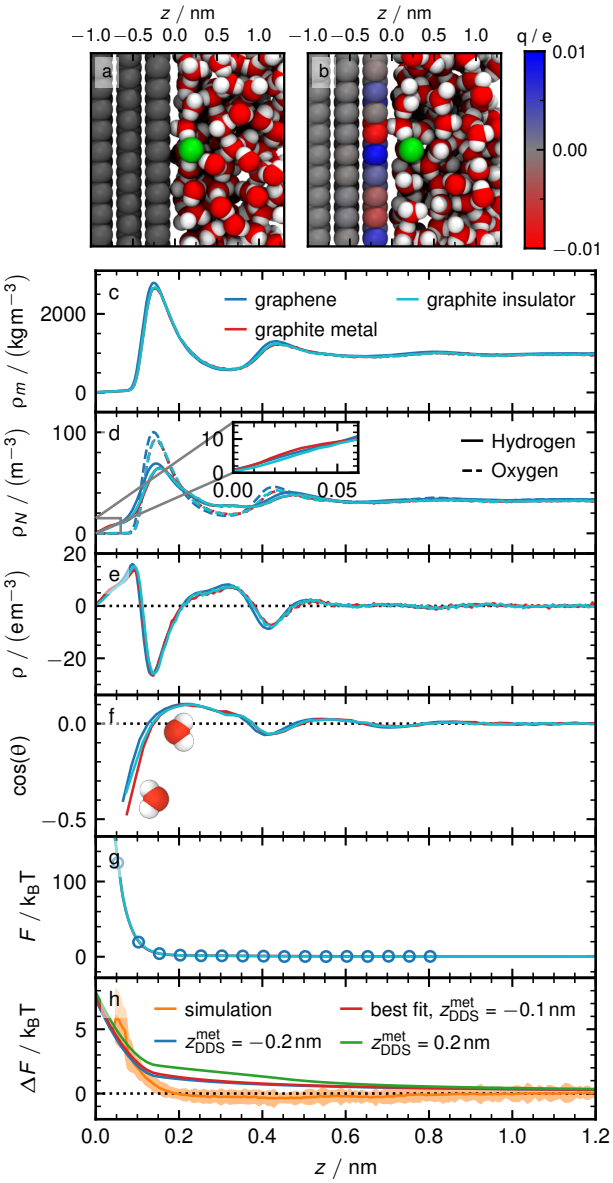

Figure 5. Snapshots for (a) the non-metallic and (b) the metallic graphite system with a chloride ion at a separation 0.2 nm from the first carbon layer. Carbon atoms are colored according to their instantaneous charge. Profiles for graphene (blue), non-metallic (light blue), and metallic (red) graphite: (c) mass density $\rho_m(z)$, (d) number density ρ_N of the hydrogen (solid line, divided by two) and oxygen atoms (dashed line), (e) charge density ρ, (f) angle between the water dipole and the z axis, $\cos\theta$, (g) chloride free energy F. (h) Difference between the chloride free energy for the non-metallic and the metallic graphite ΔF, defined in eq. (3). Simulation data (orange line) are compared to predictions from a two-region isotropic dielectric model for a spherical charged shell with finite radius according to eq. (4) with fixed $z^{\rm non}_{\rm DDS} = -0.1\,$nm. Different colors correspond to different positions of the dielectric dividing surface position for the metallic graphite $z^{\rm met}_{\rm DDS}$, obtained by fitting the model to the simulation data (red line) and for two other fixed values (blue and green lines).

chloride ion that approaches metallic graphite (red solid line) and non-metallic graphite (cyan solid line), obtained from Umbrella Sampling (see SI section S1 E), note that the red solid line is almost completely hidden behind the cyan solid line. The free-energy profile for the non-metallic graphene obtained from TI is also shown (data points). A very large free-energetic repulsion is found close to the surface. In line with our results for the interfacial water properties in Fig. 5c-f, no difference can be discerned between the free-energy profiles in Fig. 5g, which is somewhat surprising since one would, based on continuum dielectric theory, expect image-charge repulsion from the non-metallic graphite and image-charge attraction to the metallic graphite surface.

To bring out small deviations between the chloride free energy at metallic and non-metallic graphite, we show in Figure 5h the free-energy difference

$$\Delta F(z) = F_{\rm non}(z) - F_{\rm met}(z). \tag{3}$$

As expected, this difference is positive, meaning that the ion is repelled more from the non-metallic surface than from the metallic surface, but the free energy difference is rather small compared to the total free energy and only amounts to roughly 5 %. At the short distances where $\Delta F(z)$ is sizable, for $z < 0.1$ nm, the water is depleted from the surface and the water density in Fig. 5c is practically zero. However, this does not mean that the dielectric effect of the interfacial water at graphite is absent, since dielectric effects are rather long-ranged and the DDS positions of both parallel and perpendicular dielectric profiles at graphene in Fig. 1 are negative and thus the interfacial water exhibits a positive dielectric excess.

Since the LJ parameters of the metallic and non-metallic graphite surfaces are the same, $\Delta F(z)$ must be caused by electrostatic polarization effects. In order to understand the results in Fig. 5h in more depth, we compare with a dielectric continuum model for the interaction of a charged sphere with a sharp dielectric interface [39]. The radius of the sphere $a = 0.254\,$nm used in the model reflects the effective linear dielectric radius of a chloride ion and is defined by the linear Born model [38]. We neglect the tensorial character of the interfacial water dielectric response here and use an isotropic model with two dielectric constants, ε_1 for the surface and ε_2 for the water. We set $\varepsilon_1 = \infty$ for metallic graphite and $\varepsilon_1 = 1$ for non-metallic graphite and use $\varepsilon_2 = 70$, which corresponds to the dielectric constant of the SPC/E water model [55]. This simple isotropic dielectric model predicts the free-energy difference as

$$\Delta F(z) = U_{\rm iso}\left(\lambda^{\rm non}, \frac{z - z^{\rm non}_{\rm DDS}}{a}\right) - U_{\rm iso}\left(\lambda^{\rm met}, \frac{z - z^{\rm met}_{\rm DDS}}{a}\right), \tag{4}$$

where $U_{\rm iso}(\lambda, z)$ is the free energy profile of a charged spherical shell at a sharp dielectric interface, given in

eq. (S5) and first derived in Ref. 39, and $\lambda = (\epsilon_2 - \epsilon_1)/(\epsilon_1 + \epsilon_2)$ is the dielectric contrast. $z_{\rm DDS}^{\rm non}$ and $z_{\rm DDS}^{\rm met}$ are the positions of the DDS for the non-metallic and metallic graphite-water interfaces. Our neglect of the interfacial tensorial dielectric properties is justified, since it was shown for non-metallic surfaces that the polarization free energy for a tensorial dielectric 3-region model, with an anisotropic dielectric layer between $z_{\rm DDS,\perp}$ and $z_{\rm DDS,\parallel}$, agrees well with a much simpler isotropic dielectric 2-region model with the DDS position given by $z_{\rm DDS} = (z_{\rm DDS,\perp} + z_{\rm DDS,\parallel})/2$ (see Fig. S5 in the supplemental information) [38]. We thus take for the DDS at the non-metallic graphite the value for non-metallic graphene from Fig. 1e–f, approximately given by $z_{\rm DDS}^{\rm non} = -0.11\,$nm (taken as the mean of the parallel and perpendicular DDS positions). For the metallic graphite, we cannot extract the dielectric interfacial properties from our simulations, because of the limited simulation length of the constant potential simulations which is caused by their high additional computational cost. Therefore, we treat $z_{\rm DDS}^{\rm met}$ as a fitting parameter. The best non-linear least-square fit of eq. (4) over the whole z range yields $z_{\rm DDS}^{\rm met} = -0.1\,$nm and is shown in Fig. 5h as a red solid line. The pronounced deviations from the simulation data are presumably due to non-linear dielectric effects, which are neglected in the model but are present in the simulations, as we show in the next section. Most strikingly, we find that $z_{\rm DDS}^{\rm met} \approx z_{\rm DDS}^{\rm non}$, meaning that the dielectric properties of the interfacial water are suggested to be the same on the metallic and non-metallic graphite surfaces. This is surprising at first sight but totally in line with the fact that all water structural properties in Fig. 5c-f are almost indistinguishable on the metallic and non-metallic graphite surfaces. As a matter of fact, the precise position of the DDS $z_{\rm DDS}^{\rm met}$ has only a minor influence on the polarization free energy difference $\Delta F(z)$, as shown by the additional curves in Fig. 5h where we choose $z_{\rm DDS}^{\rm met} = \pm 0.2$ nm.

We note that, different from the behavior we here observe for a chloride ion on graphite, sodium ions in a 1 molar sodium chloride solution have been shown to adsorb quite strongly onto metallic gold surfaces [54, 56]. This different behavior presumably is linked to the sodium ion being smaller than chloride, but most likely also to the different parametrization of the metallic surface in those studies: in Ref. 54 a Drude-oscillator model was used, while in Ref. 56 sodium adsorption was only observed for a large Gaussian width used to characterize the spatial polarization charge distribution of the metallic surface atoms, corresponding to the rather small hardness of gold atoms. The hardness of carbon atoms is higher than that of gold atoms, and the parametrization of the present work was previously shown to reproduce experimental data [57]. In line with our results, Ref. 56 also finds only marginal differences in the water structure on metallic and non-metallic surfaces, which supports our finding that metallicity is only relevant for ions very close to the surface [58].

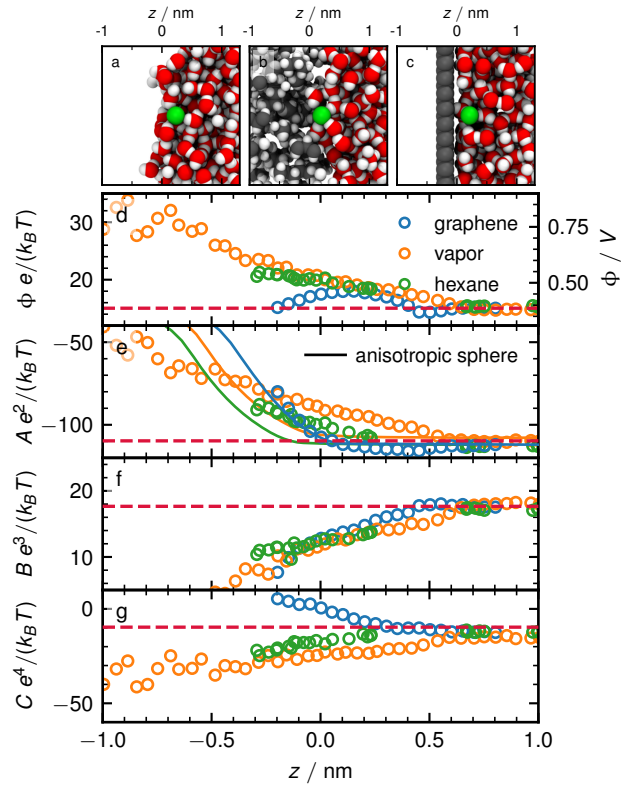

Figure 6. Simulation snapshots for (a) the vapor-liquid water system, (b) the hexane-water system, (c) the graphene-water system with a chloride ion at a position $z = 0.2\,$nm relative to the GDS. (d–g) Coefficients of the non-linear electrostatic free energy profile defined in eq. (5), obtained from fits of the Coulomb part of the simulated free energy shown in Figure S4 in the supplemental information. The horizontal red dashed lines indicate corresponding results for a chloride ion in a periodic bulk water box. The solid lines in (e) show the analytical results for a three-region tensorial dielectric model.

Non-linear dielectric effects

It is well-known that ion hydration is asymmetric and non-linear in the ion charge [38, 59–63]. To resolve this asymmetry and non-linearity as an ion approaches an interface, we determine the linear and non-linear parts of the electrostatic free energy by expanding $F_{\rm Coul}(z)$ in powers of the ion charge q

$$F_{\rm Coul}(z) = \Phi(z)q + A(z)q^2 + B(z)q^3 + C(z)q^4\,, \qquad (5)$$

where we extract the z-dependent coefficients by polynomial fits to our simulation data [38]. Details on the method and exemplary fits are shown in section S1 and Figure S4 in the supplemental information. In Fig. 6 we show the resulting coefficients for the graphene, vapor

and hexane systems as a function of the distance z of the ion from the GDS. Obviously, the coefficients for the different surfaces decay to the same values at a distance less than a nanometer from the interface and agree with results from independent bulk simulations, indicated by red dashed lines. Figure 6d shows the linear coefficient, which corresponds to the electrochemical potential $\Phi(z)$ and is defined with respect to a reference position in vacuum, which exhibits only mild deviations between the different interfaces if the ion is in the water phase, i.e. for $z > 0$. Note that $\Phi(z)$ in Fig. 6d differs substantially from $\varphi(z)$ in Fig. 1, since $\varphi(z)$ corresponds to the laterally averaged electrostatic potential in the water phase while $\Phi(z)$ is the potential inside a LJ sphere, which receives substantial contributions from the perturbed water structure around it. A more detailed comparison between $\varphi(z)$ and $\Phi(z)$ is presented in Fig. S7 in the supplemental information.

Fig. 6e shows the prefactor of the electrostatic part that is proportional to the squared ion charge q^2, $A(z)$. Here we observe rather pronounced deviations between the different surfaces even within the water phase. For $z > 0$, $A(z)$ is substantially higher for the vapor-liquid interface than for hexane and graphene, pointing to more pronounced linear dielectric repulsion from the vapor phase compared to hexane or graphene. Since $A(z)$ reflects the linear dielectric contribution to the polarization free energy, it is this part that can be compared with predictions from continuum linear dielectric theory. We therefore add results from the analytical solution of Poisson's equation using a 3-region anisotropic dielectric model that accounts for different positions of the perpendicular and parallel DDS [38], which are taken from Fig. 1. As demonstrated before [38], the 3-region anisotropic dielectric model predictions agree nicely with the simulations for the graphene system, but the model is not able to quantitatively reproduce the simulation results for the hexane-water system and even less so for the vapor-water system. The disagreement presumably originates from interfacial broadening of the dielectric profiles for the fluid-fluid interfaces, shown in Fig. 1, which is not covered in the analytical model that assumes sharp dielectric interfaces.

Figure 6f shows the prefactor $B(z)$ of the cubic dielectric contribution that is proportional to q^3, which is remarkably similar for all three interfaces (similar to the potential $\Phi(z)$ in Fig. 6d). By symmetry, this term reflects dielectric non-linear effects that are odd with respect to the sign of the ion charge. We thus conclude that the position-dependence of the $B(z)$ profile results from the non-linear coupling of the local water orientation around the ion with the water ordering at the planar interface, which seems to be rather similar in magnitude for the three different interfacial systems and does not seem to be affected much by the different broadening of the interfacial dielectric profiles shown in Fig. 1 (which should produce an effect that is even in the ion charge). In contrast, the prefactor $C(z)$ of the quartic contribution that is proportional to q^4 shows pronounced deviations between the different interface types, similar to the quadratic term $A(z)$. In fact, because $C(z)$ is very different for graphene on the one hand and the two soft interfaces on the other, we conclude that $C(z)$ reflects the capability of the water interface to deform in response to the presence of an ion. We note that our fits become unstable for ion positions far in the non-aqueous phase for $z < -1.0$ nm, presumably due to the formation of a highly volatile and fluctuating water finger around the ion [28] (see Fig. S4 in the SI for details). Thus, when a long water finger is present, a 4th-order polynomial is not sufficient to accurately describe non-linear interfacial dielectric effects.

CONCLUSION

We investigate the dielectric properties of interfacial water and the free energy profile of a chloride ion at different hydrophobic surfaces, ranging from soft, such as the vapor-liquid water interface and the hexane-water interface, to rigid, like graphene and graphite. We also consider two different versions of graphite, a metallic and a non-metallic one. This wide range of considered systems allows us to separately study the effects of surface rigidity and metallicity on the dielectric and electrostatic properties at hydrophobic-water interfaces.

We find that at soft interfaces, the interfacial water roughness and (to a lesser extent) capillary waves broaden the interfacial mass, charge density, dielectric, and electrostatic potential profiles. As a consequence, effective continuum models that employ a sharp dielectric boundary do not work well for soft interfaces, even when exclusively trying to model the linear dielectric response. In contrast, at the rigid graphene surface, all these profiles exhibit pronounced layering effects and the dielectric profiles are strongly anisotropic. The dielectric excess, quantified by the shift between the dielectric dividing surface position relative to the Gibbs dividing surface, is positive for all considered surfaces but differs significantly between the different surfaces. This means that water at hydrophobic surfaces has a higher dielectric response than in bulk, but this excess is highly surface-type specific. This dielectric surface specificity can be accounted for in continuum dielectric models by proper positioning of the dielectric dividing surface position.

The free-energy profile of a chloride ion is characterized by strong repulsion from the low-dielectric surfaces, which is dominated by electrostatics for the soft surface but by Lennard-Jones repulsion for the rigid surfaces. This has far-reaching consequences for the correct modeling of ion-surface interactions in coarse-grained models. Chloride and sodium ions in vapor and hexane are hy-

drated and surrounded by roughly 5–10 water molecules in equilibrium, which drastically lowers their free energy in the non-aqueous phase.

Comparing non-metallic and metallic graphite, we find only minute changes in the interfacial water density and orientation profiles. Also, there are only insignificant differences of the chloride free energy profiles between non-metallic and metallic graphite, which is rationalized by the fact that the repulsion is dominated by non-electrostatic interactions at a rigid surface; the small free energy difference can be modeled by a dielectric model that correctly accounts for the dielectric-dividing surface positions at the two different surfaces. Non-linear dielectric effects are pronounced at all surfaces and describe non-linear hydration effects as well as non-linear interface-deformation effects at the soft interfaces. Linear tensorial dielectric theory with sharp dielectric interfaces works well for the graphene-water interface but not for the diffuse vapor-water and hexane-water interfaces.

AUTHORS' CONTRIBUTIONS

P.L. and L.S. contributed equally to this work.

ACKNOWLEDGMENTS

We acknowledge support by Deutsche Forschungsgemeinschaft Grant IRTG-2662 project number 434130070 "Charging into the future", the MaxWater initiative from the Max-Planck Society and by the European Research Council under the European Union's Horizon 2020 research and innovation program (Grant Agreements No. 835117 and 863473). We gratefully acknowledge computing time on the HPC clusters at the physics department and ZEDAT, FU Berlin.

DATA AVAILABILITY

The data that support the findings of this study are available upon reasonable request. The code used for the constant potential simulations is openly available in the repository `https://gitlab.com/ampere2/metalwalls`.

* rnetz@physik.fu-berlin.de

[1] J. Israelachvili and H. Wennerström, Role of hydration and water structure in biological and colloidal interactions, Nature 10.1038/379219a0 (1996).

[2] O. Teschke, G. Ceotto, and E. F. de Souza, Interfacial water dielectric-permittivity-profile measurements using atomic force microscopy, Physical Review E **64**, 011605 (2001), publisher: American Physical Society.

[3] H. A. Stern and S. E. Feller, Calculation of the dielectric permittivity profile for a nonuniform system: Application to a lipid bilayer simulation, J. Chem. Phys. 10.1063/1.1537244 (2003).

[4] J. Faraudo and F. Bresme, Anomalous Dielectric Behavior of Water in Ionic Newton Black Films, Phys. Rev. Lett. 10.1103/PhysRevLett.92.236102 (2004).

[5] V. Ballenegger and J.-P. Hansen, Dielectric permittivity profiles of confined polar fluids, The Journal of Chemical Physics **122**, 114711 (2005), publisher: American Institute of Physics.

[6] D. J. Bonthuis, S. Gekle, and R. R. Netz, Profile of the static permittivity tensor of water at interfaces: Consequences for capacitance, hydration interaction and ion adsorption, Langmuir 10.1021/la2051564 (2012).

[7] D. Muñoz-Santiburcio and D. Marx, Nanoconfinement in Slit Pores Enhances Water Self-Dissociation, Phys. Rev. Lett. 10.1103/PhysRevLett.119.056002 (2017).

[8] L. Fumagalli, A. Esfandiar, R. Fabregas, S. Hu, P. Ares, A. Janardanan, Q. Yang, B. Radha, T. Taniguchi, K. Watanabe, G. Gomila, K. S. Novoselov, and A. K. Geim, Anomalously low dielectric constant of confined water, Science 10.1126/science.aat4191 (2018).

[9] P. Loche, C. Ayaz, A. Wolde-Kidan, A. Schlaich, and R. R. Netz, Universal and Nonuniversal Aspects of Electrostatics in Aqueous Nanoconfinement, J. Phys. Chem. B 10.1021/acs.jpcb.0c01967 (2020).

[10] A. Montenegro, C. Dutta, M. Mammetkuliev, H. Shi, B. Hou, D. Bhattacharyya, B. Zhao, S. B. Cronin, and A. V. Benderskii, Asymmetric response of interfacial water to applied electric fields, Nature **594**, 62 (2021), number: 7861 Publisher: Nature Publishing Group.

[11] S. Mondal and B. Bagchi, Anomalous dielectric response of nanoconfined water, The Journal of Chemical Physics **154**, 044501 (2021), publisher: American Institute of Physics.

[12] G. Gonella, E. H. G. Backus, Y. Nagata, D. J. Bonthuis, P. Loche, A. Schlaich, R. R. Netz, A. Kühnle, I. T. McCrum, M. T. M. Koper, M. Wolf, B. Winter, G. Meijer, R. K. Campen, and M. Bonn, Water at charged interfaces, Nat Rev Chem 10.1038/s41570-021-00293-2 (2021).

[13] J. Sala, E. Guàrdia, and J. Martí, Specific ion effects in aqueous eletrolyte solutions confined within graphene sheets at the nanometric scale, Phys. Chem. Chem. Phys. 10.1039/C2CP40537G (2012).

[14] D. Muñoz-Santiburcio and D. Marx, Chemistry in nanoconfined water, Chem. Sci. 10.1039/C6SC04989C (2017).

[15] P. Jungwirth and D. J. Tobias, Specific Ion Effects at the Air/Water Interface, Chem. Rev. 10.1021/cr0403741 (2006).

[16] S. I. Mamatkulov, C. Allolio, R. R. Netz, and D. J. Bonthuis, Orientation-Induced Adsorption of Hydrated Protons at the Air–Water Interface, Angewandte Chemie International Edition 10.1002/anie.201707391 (2017).

[17] B. H. Honig, W. L. Hubbell, and R. F. Flewelling, Electrostatic interactions in membranes and proteins, Annu. Rev. Biophys. Biophys. Chem. 10.1146/annurev.bb.15.060186.001115 (1986).

[18] C. M. Starks, C. L. Liotta, and M. E. Halpern, *Phase-Transfer Catalysis* (Springer Netherlands, Dordrecht, 1994).

[19] G. Feng, S. Li, V. Presser, and P. T. Cummings, Molecular Insights into Carbon Supercapacitors Based on Room-Temperature Ionic Liquids, J. Phys. Chem. Lett. 10.1021/jz4014163 (2013).

[20] F. Valenzuela, C. Fonseca, C. Basualto, O. Correa, C. Tapia, and J. Sapag, Removal of copper ions from a waste mine water by a liquid emulsion membrane method, Minerals Engineering 10.1016/j.mineng.2004.05.011 (2005).

[21] A. C. Maggs and R. Everaers, Simulating Nanoscale Dielectric Response, Phys. Rev. Lett. 10.1103/PhysRevLett.96.230603 (2006).

[22] L. Joly, R. H. Meißner, M. Iannuzzi, and G. Tocci, Osmotic Transport at the Aqueous Graphene and hBN Interfaces: Scaling Laws from a Unified, First-Principles Description, ACS Nano 10.1021/acsnano.1c05931 (2021).

[23] A. Schlaich, E. W. Knapp, and R. R. Netz, Water Dielectric Effects in Planar Confinement, Phys. Rev. Lett. 10.1103/PhysRevLett.117.048001 (2016).

[24] D. L. McCaffrey, S. C. Nguyen, S. J. Cox, H. Weller, A. P. Alivisatos, P. L. Geissler, and R. J. Saykally, Mechanism of ion adsorption to aqueous interfaces: Graphene/water vs. air/water, Proceedings of the National Academy of Sciences **114**, 13369 (2017).

[25] H. J. C. Berendsen, J. R. Grigera, and T. P. Straatsma, The missing term in effective pair potentials, The Journal of Physical Chemistry **91**, 6269 (1987).

[26] J. S. Hub, B. L. de Groot, H. Grubmüller, and G. Groenhof, Quantifying Artifacts in Ewald Simulations of Inhomogeneous Systems with a Net Charge, J. Chem. Theory Comput. 10.1021/ct400626b (2014).

[27] S. Weerasinghe and P. E. Smith, A Kirkwood–Buff derived force field for sodium chloride in water, The Journal of Chemical Physics 10.1063/1.1622372 (2003).

[28] P. Loche, D. J. Bonthuis, and R. R. Netz, Molecular dynamics simulations of the evaporation of hydrated ions from aqueous solution, Commun Chem 10.1038/s42004-022-00669-5 (2022).

[29] S. W. I. Siu, K. Pluhackova, and R. A. Böckmann, Optimization of the OPLS-AA Force Field for Long Hydrocarbons, J. Chem. Theory Comput. 10.1021/ct200908r (2012).

[30] A. Schlaich, B. Kowalik, M. Kanduč, E. Schneck, and R. R. Netz, Simulation Techniques for Solvation-Induced Surface-Interactions at Prescribed Water Chemical Potential, in *IAS Series, Computational Trends in Solvation and Transport in Liquids* (Forschungszentrum Jülich GmbH, Zentralbibliothek, 52425 Jülich, 2015).

[31] M. J. Abraham, T. Murtola, R. Schulz, S. Páll, J. C. Smith, B. Hess, and E. Lindahl, GROMACS: High performance molecular simulations through multi-level parallelism from laptops to supercomputers, SoftwareX 10.1016/j.softx.2015.06.001 (2015).

[32] I.-C. Yeh and M. L. Berkowitz, Ewald summation for systems with slab geometry, The Journal of Chemical Physics http://dx.doi.org/10.1063/1.479595 (1999).

[33] A. Marin-Laflèche, M. Haefele, L. Scalfi, A. Coretti, T. Dufils, G. Jeanmairet, S. K. Reed, A. Serva, R. Berthin, C. Bacon, S. Bonella, B. Rotenberg, P. A. Madden, and M. Salanne, MetalWalls: A classical molecular dynamics software dedicated to the simulation of electrochemical systems, Journal of Open Source Software **5**, 2373 (2020).

[34] L. Scalfi, D. T. Limmer, A. Coretti, S. Bonella, P. A. Madden, M. Salanne, and B. Rotenberg, Charge fluctuations from molecular simulations in the constant-potential ensemble, Physical Chemistry Chemical Physics **22**, 10480 (2020).

[35] F. Sedlmeier, D. Horinek, and R. R. Netz, Spatial Correlations of Density and Structural Fluctuations in Liquid Water: A Comparative Simulation Study, J. Am. Chem. Soc. 10.1021/ja1064137 (2011).

[36] S. M. Kathmann, I.-F. W. Kuo, C. J. Mundy, and G. K. Schenter, Understanding the Surface Potential of Water, J. Phys. Chem. B 10.1021/jp1116036 (2011).

[37] M. D. Baer, A. C. Stern, Y. Levin, D. J. Tobias, and C. J. Mundy, Electrochemical Surface Potential Due to Classical Point Charge Models Drives Anion Adsorption to the Air–Water Interface, J. Phys. Chem. Lett. 10.1021/jz300302t (2012).

[38] P. Loche, C. Ayaz, A. Schlaich, D. J. Bonthuis, and R. R. Netz, Breakdown of Linear Dielectric Theory for the Interaction between Hydrated Ions and Graphene, J. Phys. Chem. Lett. 10.1021/acs.jpclett.8b02473 (2018).

[39] M. N. Tamashiro and M. A. Constantino, Ions at the Water-Vapor Interface, J. Phys. Chem. B 10.1021/jp911898t (2010).

[40] S. Garde, G. Hummer, A. E. García, M. E. Paulaitis, and L. R. Pratt, Origin of Entropy Convergence in Hydrophobic Hydration and Protein Folding, Physical Review Letters **77**, 4966 (1996).

[41] D. M. Huang and D. Chandler, Temperature and length scale dependence of hydrophobic effects and their possible implications for protein folding, Proceedings of the National Academy of Sciences **97**, 8324 (2000).

[42] F. Sedlmeier, D. Horinek, and R. R. Netz, Entropy and enthalpy convergence of hydrophobic solvation beyond the hard-sphere limit, The Journal of Chemical Physics **134**, 055105 (2011).

[43] l. Benjamin, Mechanism and Dynamics of Ion Transfer Across a Liquid-Liquid Interface, Science 10.1126/science.261.5128.1558 (1993).

[44] J. J. Karnes and I. Benjamin, Geometric and energetic considerations of surface fluctuations during ion transfer across the water-immiscible organic liquid interface, The Journal of Chemical Physics 10.1063/1.4954331 (2016).

[45] M. Darvas, M. Jorge, M. N. D. S. Cordeiro, S. S. Kantorovich, M. Sega, and P. Jedlovszky, Calculation of the Intrinsic Solvation Free Energy Profile of an Ionic Penetrant Across a Liquid–Liquid Interface with Computer Simulations, J. Phys. Chem. B 10.1021/jp404699t (2013).

[46] C. Caleman, J. S. Hub, P. J. van Maaren, and D. van der Spoel, Atomistic simulation of ion solvation in water explains surface preference of halides, PNAS 10.1073/pnas.1017903108 (2011).

[47] D. R. Lide, *CRC Handbook of Chemistry and Physics, 85th Edition* - (CRC Press, Boca Raton, Fla, 2004).

[48] J. Polak and B. C.-Y. Lu, Mutual Solubilities of Hydrocarbons and Water at 0 and 25 °C, Canadian Journal of Chemistry **51**, 4018 (1973).

[49] R. Fuentes-Azcatl and J. Alejandre, Non-Polarizable Force Field of Water Based on the Dielectric Constant: TIP4P/epsilon, J. Phys. Chem. B 10.1021/jp410865y (2014).

[50] S. Liese, M. Gensler, S. Krysiak, R. Schwarzl, A. Achazi, B. Paulus, T. Hugel, J. P. Rabe, and R. R. Netz, Hydration Effects Turn a Highly Stretched Polymer

from an Entropic into an Energetic Spring, ACS Nano 10.1021/acsnano.6b07071 (2017).

[51] T. A. Ho and A. Striolo, Polarizability effects in molecular dynamics simulations of the graphene-water interface, The Journal of Chemical Physics **138**, 054117 (2013).

[52] L. Scalfi, T. Dufils, K. G. Reeves, B. Rotenberg, and M. Salanne, A semiclassical Thomas–Fermi model to tune the metallicity of electrodes in molecular simulations, The Journal of Chemical Physics **153**, 174704 (2020).

[53] S. Ntim and M. Sulpizi, Role of image charges in ionic liquid confined between metallic interfaces, Physical Chemistry Chemical Physics **22**, 10786 (2020).

[54] Z. Li, V. G. Ruiz, M. Kanduč, and J. Dzubiella, Highly Heterogeneous Polarization and Solvation of Gold Nanoparticles in Aqueous Electrolytes, ACS Nano **15**, 13155 (2021).

[55] M. Rami Reddy and M. Berkowitz, The dielectric constant of SPC/E water, Chemical Physics Letters **155**, 173 (1989).

[56] A. Serva, L. Scalfi, B. Rotenberg, and M. Salanne, Effect of the metallicity on the capacitance of gold–aqueous sodium chloride interfaces, The Journal of Chemical Physics **155**, 044703 (2021).

[57] M. Simoncelli, N. Ganfoud, A. Sene, M. Haefele, B. Daffos, P.-L. Taberna, M. Salanne, P. Simon, and B. Rotenberg, Blue Energy and Desalination with Nanoporous Carbon Electrodes: Capacitance from Molecular Simulations to Continuous Models, Physical Review X **8**, 021024 (2018).

[58] G. Pireddu, L. Scalfi, and B. Rotenberg, A molecular perspective on induced charges on a metallic surface, The Journal of Chemical Physics **155**, 204705 (2021), publisher: American Institute of Physics.

[59] R. M. Lynden-Bell and J. C. Rasaiah, From hydrophobic to hydrophilic behaviour: A simulation study of solvation entropy and free energy of simple solutes, The Journal of Chemical Physics 10.1063/1.474550 (1997).

[60] S. Rajamani, T. Ghosh, and S. Garde, Size dependent ion hydration, its asymmetry, and convergence to macroscopic behavior, The Journal of Chemical Physics 10.1063/1.1644536 (2004).

[61] J. P. Bardhan, P. Jungwirth, and L. Makowski, Affine-response model of molecular solvation of ions: Accurate predictions of asymmetric charging free energies, J Chem Phys 10.1063/1.4752735 (2012).

[62] S. J. Cox, D. G. Thorpe, P. R. Shaffer, and P. L. Geissler, Assessing long-range contributions to the charge asymmetry of ion adsorption at the air–water interface, Chem. Sci. 10.1039/D0SC01947J (2020).

[63] S. J. Cox, K. K. Mandadapu, and P. L. Geissler, Quadrupole-mediated dielectric response and the charge-asymmetric solvation of ions in water, J. Chem. Phys. 10.1063/5.0051399 (2021).